



Finite Element Analysis of Weld Residual Stresses in Austenitic Stainless Steel Dry Cask Storage System Canisters

Technical Letter Report

Joshua Kusnick¹, Michael Benson¹, and Sara Lyons²

U.S. Nuclear Regulatory Commission

¹Office of Nuclear Regulatory Research

²Office of Nuclear Reactor Regulation

December 2013

Executive Summary

In the U.S., spent nuclear fuel (SNF) is maintained at independent spent fuel storage installations (ISFSIs). These sites are licensed by the U.S. Nuclear Regulatory Commission under title 10 of the Code of Federal Regulations, Part 72. The SNF is confined in dry cask storage systems (DCSSs), which are most commonly constructed of welded austenitic stainless steel canisters emplaced within concrete shielding structures. These shielding structures have vents to allow for convective cooling and, consequently, expose the canister surface to chlorides if they are present in the atmosphere. Chloride salts that deposit on the canister surface can deliquesce in specific environments, resulting in the aqueous solution necessary to initiate chloride-induced stress corrosion cracking (SCC) if tensile stresses are present. While tensile stresses are thought to exist on the canister surface due to forming and welding operations, the magnitude of these stresses is unknown. This report documents the analysis of the weld-induced residual stresses that could promote chloride-induced SCC initiation and growth. The modeling was conducted via a sequentially coupled thermal-structural finite element analysis for a generic canister configuration, and the report details the analytical methods, assumptions, potential implications, uncertainties, and further potential research areas. Given the welding, fabrication, and modeling assumptions imposed in this analysis, sufficiently high tensile residual stresses exist in the canister welds and their associated heat affected zones to allow for SCC initiation and potential through-wall growth if exposed to a corrosive environment.

Table of Contents

Executive Summary	i
Table of Contents.....	ii
List of Figures	iii
List of Tables	iv
1. Introduction	1
2. Background	2
2.1 Instances of CISCC	2
2.2 Weld Residual Stress Research	3
3. Canister Representative Geometry.....	3
3.1 Fabrication and Weld Processes	4
4. Weld Residual Stress Finite Element Modeling Procedure	6
4.1 Material Properties	7
4.2 Thermal Model	9
4.3 Structural Model	10
5. Benchmarking Analysis	12
5.1 Literature Review	12
5.2 Axial Stress	14
5.3 Hoop Stress	15
6. Canister WRS Analysis Results.....	16
6.1 Circumferential Weld	16
6.1.1 Axial Stress	16
6.1.2 Hoop Stress	18
6.2 Longitudinal Weld.....	20
6.2.1 Axial Stress	20
6.2.2 Hoop Stress	22
6.3 Base Plate Weld.....	24
6.4 Lid Closure Weld	27
7. Summary.....	30
References	31

List of Figures

Figure 1: 3D representation of longitudinal butt welds (dashed lines) and circumferential butt weld (solid line)	5
Figure 2: Weld sequence for longitudinal and circumferential canister welds	5
Figure 3: Left: Base plate weld sequence; Right: Lid closure weld sequence. Note: These two images are not displayed with the same scale.	6
Figure 4: Left: Sample heat input function; Right: Longitudinal weld pass-5 heat-up temperature profile.....	10
Figure 5: Left: 2D longitudinal weld model with radial constraint surfaces indicated by radial lines and circled in red, weld area indicated by green circle, pinned nodes indicated by blue square; Right: 2D circumferential weld model with radial constraint surfaces highlighted by red circles, pinned nodes indicated by blue squares. 3D representation is displayed for reference.	11
Figure 6: Benchmarking model weld geometry BA.....	13
Figure 7: Pipe benchmarking weld residual axial stress comparison	14
Figure 8: Pipe benchmarking weld residual hoop stress comparison	15
Figure 9: Circumferential weld residual axial stress contour without radial constraints; Left: Isotropic hardening; Right: Kinematic Hardening.....	17
Figure 10: Circumferential weld residual axial stress contour with radial constraints; Left: Isotropic hardening; Right: Kinematic Hardening.....	17
Figure 11: Circumferential weld residual hoop stress contour without radial constraints; Left: Isotropic hardening; Right: Kinematic Hardening.....	18
Figure 12: Circumferential weld residual hoop stress contour with radial constraints; Left: Isotropic hardening; Right: Kinematic Hardening.....	19
Figure 13: Paths along which through-wall stresses are plotted for the circumferential and longitudinal canister butt welds	19
Figure 14: Circumferential Weld Through-Wall Residual Stress; Left: With radial constraints; Right: Without radial constraints.....	20
Figure 15: Longitudinal weld residual axial stress; Top to bottom: (1) Without radial constraints, isotropic hardening; (2) Without radial constraints, kinematic hardening; (3) With radial constraints, isotropic hardening; (4) With radial constraints, kinematic hardening	21
Figure 16: Longitudinal weld residual hoop stress; Top to bottom: (1) Without radial constraints, isotropic hardening; (2) Without radial constraints, kinematic hardening; (3) With radial constraints, isotropic hardening; (4) With radial constraints, kinematic hardening	22
Figure 17: Longitudinal weld through-wall residual stress; Left: With radial constraints; Right: Without radial constraints	23
Figure 18: Paths for Base Plate Stress Plots.....	24
Figure 19: Base plate weld contours; Left: Isotropic Hardening; Right: Kinematic Hardening	25
Figure 20: Base plate stress along paths: (a) Through-weld; (b) Base plate outer surface; (c) Cask wall outer surface	26
Figure 21: Paths for Lid Stress Plots	27
Figure 22: Lid weld contours; Left: Isotropic Hardening; Right: Kinematic Hardening	28
Figure 23: Lid stress along paths: (a) Through-weld; (b) Lid outer surface; (c) Cask wall outer surface.....	29

List of Tables

Table 1: CISC in nuclear power plant components exposed to atmospheric conditions near salt water bodies	2
Table 2: Thermal Material Properties	7
Table 3: Mechanical Material Properties and Isotropic Hardening Law Inputs	8
Table 4: Kinematic Material Hardening Properties	9

1. Introduction

Instances of chloride-induced SCC due to atmospheric exposure of low operating pressure, near ambient temperature austenitic stainless steel components at various operating nuclear power plants have led to through-wall failures in the weld heat affected zone [1]. SCC requires a corrosive environment, a susceptible material, and tensile stress in the material. More than 1300 austenitic stainless steel DCSS canisters are in service in the U.S., and many of these are located at sites where they may be exposed to airborne chloride salts via external vents [2]. A corrosive environment can result from the deliquescence of these salts, a process which is dependent on factors such as humidity, salt deposit concentration, and temperature [3]. Previous studies showed that austenitic stainless steels, including the types 304 and 316 commonly used for DCSS canister construction, can be susceptible to SCC when exposed to atmospheric chlorides [4]. Furthermore, SCC occurred in type 304, 304L, and 316L stainless steel U-bend test specimens undergoing chloride-induced SCC testing within the natural range of atmospheric absolute humidity, even when exposed to relatively low chloride salt concentrations [3]. Additionally, ongoing testing on C-ring specimens with more realistic strain states (strained to yield stress, ~0.3% plastic strain, or to 1.5% plastic strain) showed pitting and SCC initiation [5]. It is therefore necessary to quantify the stress state in a storage canister to correlate laboratory testing of U-bend and C-ring specimens to DCSS canister conditions.

Because DCSS canisters are not significantly pressurized, the main source of stress is likely to arise from fabrication and weld residual stresses, which are primary drivers of SCC in piping butt welds of pressurized water reactors [6]. Therefore, quantifying and characterizing the residual stresses in DCSS canisters will aid in evaluating the potential for SCC. This report aims to obtain a more accurate quantification of the canister stress state to help relate the results of SCC coupon testing to DCSS canisters. Experimental measurements of canister weld residual stress would be beneficial to validate these finite element modeling results.

2. Background

This section describes instances of chloride-induced stress corrosion cracking (CISCC) in stainless steel components exposed to atmospheric conditions near salt-water bodies, briefly summarizes CISCC susceptibility research for DCSS canister materials, and highlights the importance of weld residual stress in SCC crack initiation and growth. It also provides a brief description of WRS modeling research upon which the methods applied in this report are derived.

2.1 Instances of CISCC

Austenitic stainless steels can experience SCC when exposed to atmospheric chlorides [1, 3, 4, 5]. Specific instances of CISCC at nuclear power plants are documented in NRC Information Notice 2012-20 [1] and are summarized in Table 1 below. Note that all of these events occurred in components with low operating pressures and temperatures, similar to those of DCSS canisters.

Table 1: CISCC in nuclear power plant components exposed to atmospheric conditions near salt water bodies

Year	Plant	Component	Event	Estimated Time	Operating Conditions
1999	St. Lucie	Type 304 SS ECCS piping	Through-wall crack (TWC) in weld HAZ	16 years exposure to outdoor environment	207 kPag (30 psig) 49°C (120°F)
2001	Koeberg NPS	Type 304L SS reactor cavity & SFP cooling system tanks	TWCs primarily adjacent to welds	16-25 yrs exposure to marine atm.	Open to atm. 7-40°C (45-104°F)
2005	Turkey Point	Type 304 SS SFP cooling line in room with grated steel door to outside env.	TWC 0.5 in. downstream of flange butt weld	N/A	1.03 MPag (150 psig) @ 100°C (<i>design</i>)
2009	San Onofre NGS	Type 304 SS ECCS piping and alternate boration piping	Three instances of TWCs in weld HAZ	25 years exposure to marine atm.	N/A

2.2 Weld Residual Stress Research

The local heating and cooling during welding produce a non-uniform temperature distribution. Typically, the weld metal and adjacent heat affected zone (HAZ) of the base metal are heated to temperatures substantially above the unaffected base metal. As the molten weld metal cools and solidifies, it shrinks, exerting stresses on the surrounding weld metal and heat affected zone. Local tensile residual stresses imparted by the welding process are a primary factor in stress corrosion cracking, and therefore there is a significant body of work in numerical methods (finite element analysis) to predict the weld residual stress (WRS) distribution in a component and validate the numerical models experimentally. Much of this work has been for dissimilar metal butt welds of large nozzles in nuclear power plant systems.

The NRC and the Electric Power Research Institute (EPRI) completed the initial phases of a WRS analysis validation program under an addendum to the Memorandum of Understanding (MOU), which allows the NRC and EPRI to perform cooperative research. The study assessed WRS predictions in pressurized water reactor primary cooling loop components containing dissimilar metal butt welds. It was carried out in four phases of increasing complexity from laboratory size specimens to component mock-ups and plant material. The findings have been documented in several reports, including [6], [7], [8], [9]. Several modelers independently provided predictions of WRS, and the results agreed reasonably well with the experimentally measured through-wall stress. However, while the overall trend of the through-wall WRS in the dissimilar metal weld was captured by modeling, there was still large analyst-to-analyst variability, and not all features of the measurement data were reflected by the models. Phase 2b of the study, currently underway, aims to reduce this uncertainty. Sources of modeling uncertainty identified included the weld process sequence, heat input, material properties, and the choice of material hardening law. These inputs are described in detail in section 4. General weld residual stress modeling guidelines for dissimilar metal welds were developed as a result of the WRS validation program[10], and they are generally adhered to in the finite element modeling procedure followed in this report. Because the typical DCSS canister weld geometry and fabrication are considerably different than primary coolant loop piping and nozzles, we performed a benchmarking analysis on a more representative example from a literature survey. The benchmarking analysis is documented in section 5.

3. Canister Representative Geometry

The current work analyzes a representative DCSS canister geometry. Canisters are cylindrical and typically have an outside diameter of 1.5 to 1.8 m, a length between 4.5 and 5.0 m, and a shell thickness in the range of 12.7 to 15.875 mm [11]. The model used in this analysis has an outside diameter of 1.7 m, a length of 4.73 m, and a shell thickness of 15.875 mm. We assigned the same thermo-physical and mechanical material properties for stainless steel to both the weld and canister base materials. Separate analyses applied isotropic and kinematic strain-hardening laws, and resulting two-dimensional contours and through-wall weld residual stress components in the hoop and axial directions are presented.

3.1 Fabrication and Weld Processes

We assumed the following process for the construction of a representative canister:

- a. An austenitic stainless steel sheet is cold rolled to form a cylinder.
- b. A longitudinal weld is applied to maintain the cylindrical shape.
- c. Two cylinders are then joined end-to-end by a circumferential weld.
- d. Another circumferential weld secures the circular bottom plate to the canister.
- e. Finally the circumferential lid closure weld is applied.

We modeled each of the four different welds required for construction: the longitudinal weld, circumferential weld, base plate weld, and lid-closure weld. In some cases repair welds may also be important contributors to tensile residual stress, but they are not included in this analysis. While all analyses are two dimensional, three dimensional representations of the circumferential and longitudinal welds are shown for illustrative purposes (Figure 1).

Various joint configurations and welding processes are used to fabricate DCSS canisters. In this analysis, a double-V butt joint configuration is used for both the longitudinal and circumferential canister welds. The weld geometry and sequence is shown in Figure 2. Two weld passes are completed on the inside surface of the cylinder, a back-gouge machining process is simulated from the outer surface by removing the elements shown in red in the upper right image of Figure 2, and then three weld passes are applied from the outer surface. The base plate weld is also of a double-V configuration, with six inner passes to accommodate the thicker 1.75 inch plate, and three outer passes. The lid is 1.25 inches thick and is secured with a single-V closure weld consisting of three passes. The base plate and lid closure weld geometry and sequence are shown in Figure 3. Note that all models contained the full two-dimension wall profile of the canister, but the weld images are cropped to isolate the welded section.

Two-dimensional weld bead shapes, or profiles, can be obtained from mockups using laser profilometry measurements performed after each weld pass, or less preferably, from an etched cross-section of the completed weld [6]. Because the work in this paper is purely analytical and real canister weld cross-sections were not available, weld bead profiles were estimated. It has been shown for thick structures that matching the precise bead cross-section used in practice is not necessary for obtaining accurate results; rectangular bead cross-sections, for instance, have been shown to provide sufficient accuracy when compared to rounded profiles [7], [10]. However, for the analysis of thin-walled cylinders with relatively few weld passes, bead shape may have a larger effect on the results. The number of weld passes, order of bead deposition, and fabrication sequence are important parameters in the residual stress analysis [7].

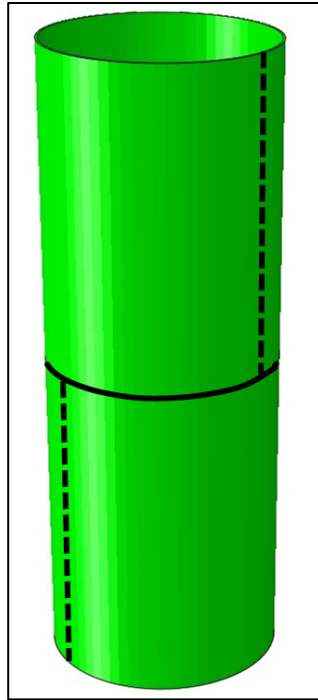


Figure 1: 3D representation of longitudinal butt welds (dashed lines) and circumferential butt weld (solid line)

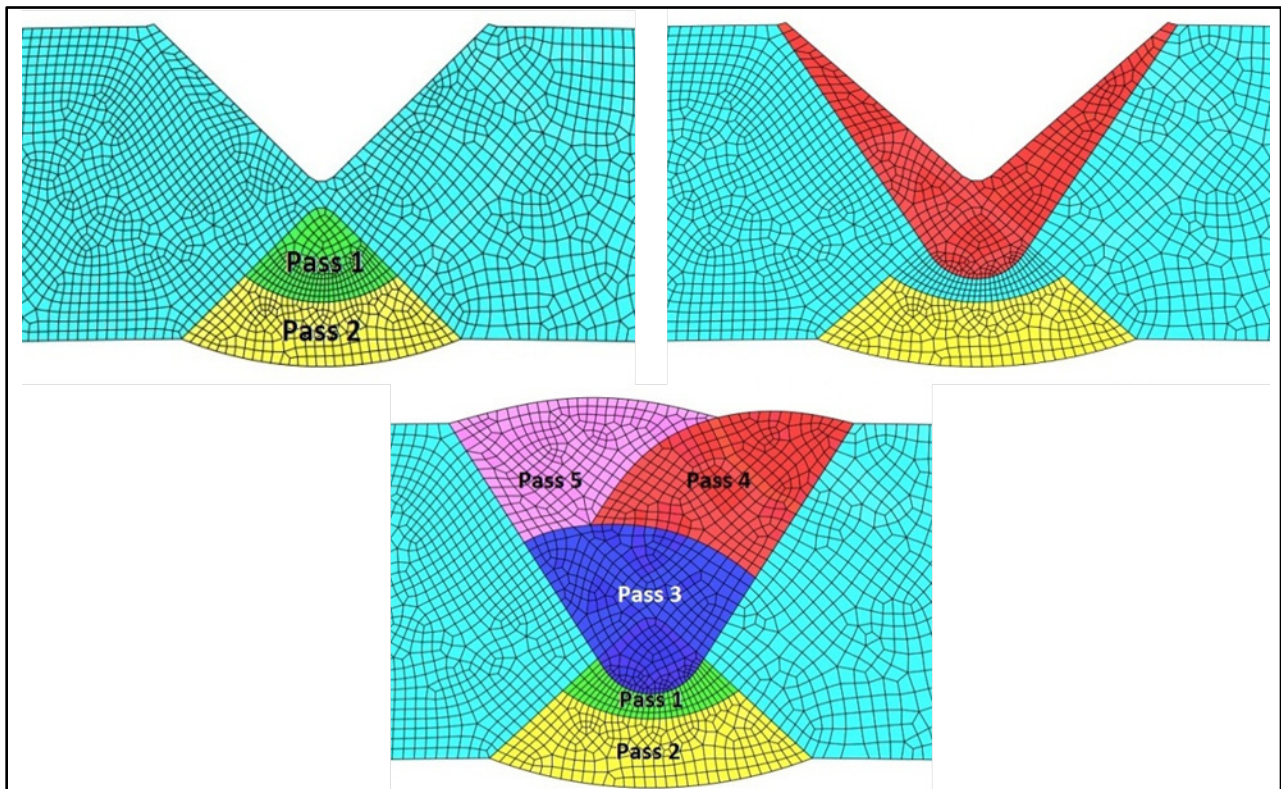


Figure 2: Weld sequence for longitudinal and circumferential canister welds

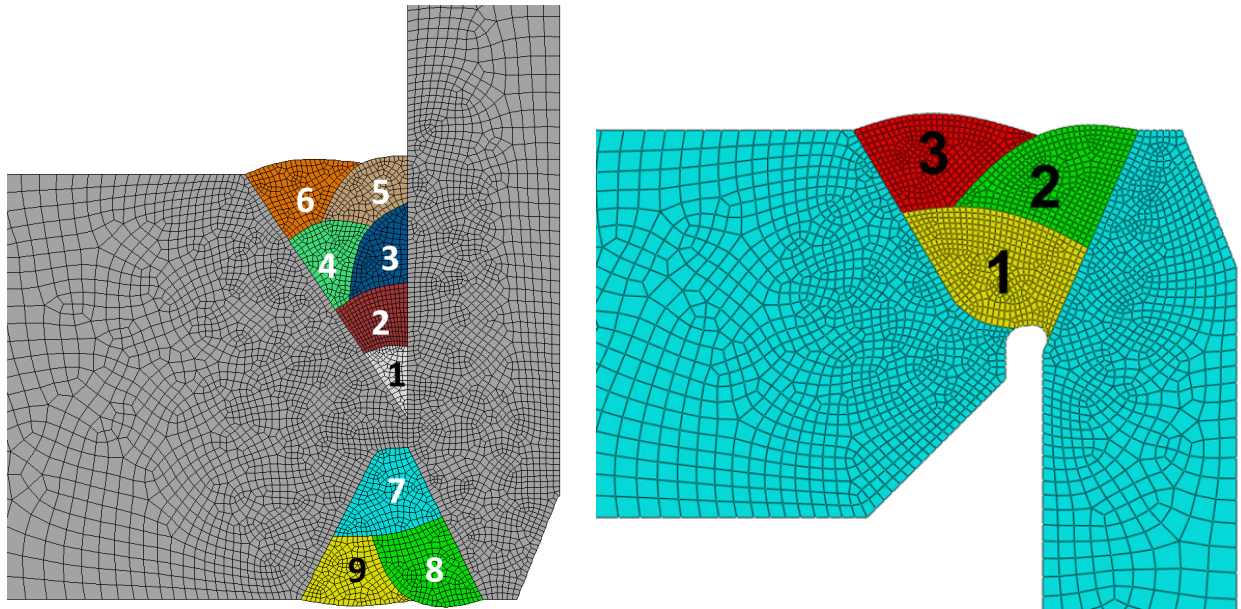


Figure 3: **Left:** Base plate weld sequence; **Right:** Lid closure weld sequence. Note: These two images are not displayed with the same scale.

4. Weld Residual Stress Finite Element Modeling Procedure

The welding residual stress model employed a two-dimensional, sequentially coupled thermal-structural analysis to analyze weld residual stresses. We performed all analyses using ABAQUS®/Standard version 6.11. Because this was a purely analytical effort without accompanying experimental measurements, we selected a benchmarking case, described in section 5, from a literature review to validate the method used herein. Specifically, we compared the trends and magnitude of the through-wall stress profiles at the weld centerline of a stainless steel circumferential pipe butt weld against analytical and experimental measurements from the comparative analysis. The method used in this report was originally developed under a previous effort concerned with dissimilar metal welds of pressure vessel nozzles [6], so we completed the benchmarking study to gauge the suitability of the analysis for the purposes of this report, which is concerned with a cylindrical geometry with stainless steel base and weld metal. The results of both the benchmarking study and the DCSS canister analyses are documented in sections 5 and 6, respectively.

We analyzed four different canister welds for this work, as described in section 3. The circumferential weld, base plate weld, and lid-closure weld models used 4-node, bilinear, axisymmetric, quadrilateral reduced integration elements. The longitudinal weld models employed 4-node, bilinear, plane-strain quadrilateral reduced integration elements. First, a thermal analysis calculated the time-dependent heat transfer solution during the welding process. Next, the temperature results were mapped to a structural model to calculate the resulting stress distribution. These models are discussed in detail below.

4.1 Material Properties

The temperature-dependent thermo-physical and mechanical properties used in this analysis are listed in Table 2, Table 3, and Table 4. The weld material and a portion of the surrounding base material are heated to elevated temperatures during the welding process. As a result, plastic deformation occurs and results in strain hardening. Therefore, material hardening inputs are required for the structural simulation.

Each structural analysis is repeated using two different hardening laws: nonlinear isotropic and kinematic. Real materials experience a mix of these two behaviors. Note that for isotropic hardening, the yield surface expands uniformly in all directions such that the yield stress increases as plastic straining occurs; hence, the last three columns of Table 3 define the yield-stress, plastic-strain relationship for a given temperature. Abaqus® implements the Lamaitre-Chaboche [12] cyclic plasticity constitutive law for nonlinear isotropic/kinematic hardening. This law permits the yield surface to both expand and translate, as seen in (1), where the size of the yield surface, σ^0 , is defined as a function of the equivalent plastic strain, temperature, and field variables (additional material parameters) that are calibrated from cyclic test data. The nonlinear kinematic hardening component, or translation of the yield surface, is governed by the parameter α , as seen in equations 1-3. The material parameters C and γ provide the best fit to the stress-strain data for each temperature. The expansion of the yield surface during cyclic loading is determined by equation 4, with parameters Q_∞ and b fit to cyclic data. For more details on the material hardening laws and parameters, see references [12-13].

Generally, analyses using an isotropic strain hardening law result in higher stresses than those applying kinematic hardening [7], and stresses calculated using mixed-mode hardening lie somewhere in between [14]. This is due to the continual increase in stress permitted by the expanding yield surface that is characterized by the isotropic hardening rule [6].

$$F = f(\sigma - \alpha) - \sigma^0 = 0 \quad (1)$$

$$\dot{\alpha} = C_k \frac{1}{\sigma^0} (\sigma - \alpha) \dot{\epsilon}^{pl} - \gamma_k \alpha_k \dot{\epsilon}^{pl} \quad (2)$$

$$\alpha = \sum_{k=1}^N \alpha_k \quad (3)$$

$$\sigma^0 = \sigma|_0 + Q_\infty (1 - e^{-b\bar{\epsilon}^{pl}}) \quad (4)$$

Table 2: Thermal Material Properties

Temperature (K)	Conductivity (W/mm-K)	Temperature (K)	Specific Heat (J/g-K)	Latent Heat (J/g)	Temperature Range (K)
300	0.0133824	360	0.3433176	40	1560-1630
700	0.02091	700	0.4856688	225	1630-1670
1200	0.033456	870	0.5359104		
2000	0.08	925	0.544284		
		1300	0.5526576		

Table 3: Mechanical Material Properties and Isotropic Hardening Law Inputs

Temperature (K)	Coefficient of Thermal Expansion (mm/mm-K)	Temperature (K)	Modulus of Elasticity (MPa)	Poisson's Ratio	Temperature (K)	Yield Stress (MPa)	Plastic Strain
296.89	1.46E-05	300	2.07E+05	2.80E-01	294	241	0.00
421.89	1.58E-05	477	1.86E+05	2.90E-01	294	290	0.01
560.78	1.68E-05	700	1.67E+05	3.00E-01	294	393	0.05
644.11	1.72E-05	922	1.45E+05	2.85E-01	294	483	0.10
755.22	1.77E-05	1144	1.14E+05	2.50E-01	294	621	0.20
866.33	1.82E-05	1366	6.21E+04	2.50E-01	294	827	0.40
977.44	1.84E-05	1477	2.76E+04	2.50E-01	693	117	0.00
1088.56	1.87E-05	1550	1.00E+04	2.50E-01	693	193	0.01
1173	1.91E-05	1728	2.00E+03	2.50E-01	693	276	0.05
1273	1.93E-05				693	359	0.10
1373	1.96E-05				693	483	0.20
1673	2.02E-05				693	621	0.40
					693	724	0.80
					923	97	0.00
					923	145	0.01
					923	214	0.05
					923	283	0.10
					923	379	0.20
					923	448	0.40
					923	483	0.80
					1089	69	0.00
					1089	110	0.01
					1089	145	0.05
					1089	172	0.10
					1089	207	0.20
					1089	241	0.40
					1089	241	0.80
					1366	28	0.00
					1366	39	0.01
					1366	41	0.05
					1366	41	0.10
					1366	41	0.20
					1366	41	0.40
					1366	41	0.80
					1550	5	0.00

Table 4: Kinematic Material Hardening Properties

Temperature (K)	Yield Stress at Zero Plastic Strain (MPa)	Hardening Parameter C_1	Hardening Parameter γ_1
293	255.3	4997	34
373	204.9	5268.2	34
473	166.2	5576.2	34
548	150.7	5726.9	34
573	147.6	5753.2	34
673	142.2	5695.7	34
773	142.7	5300.2	34
798	143	5136.4	34
873	142.2	4463.1	34
973	133.5	3080.9	34
1073	110.2	334	34
1123	89.1	159.3	34
1173	71.32	0	34
1273	34.89	0	34

4.2 Thermal Model

The two-dimensional models in this report used a static heat source for the weld pass thermal loading, and the exterior surfaces of the model geometry were treated as free convective surfaces. Because the models are two-dimensional, a moving heat source was not modeled. Rather, the weld bead was applied along the entire surface of the part at once. To simulate the heating and cooling of a weld bead as it is applied, the weld elements were prescribed a heat flux that exponentially increased, then decreased, for a designated period of time. The method is based on a moving heat source model originally developed by Goldak [15] and modified for 2D geometry [16]-[18]. The energy input per unit time, or power density, Q , is modeled as

$$Q = K \exp\left\{-\frac{[t - (1 + a_0)]^2}{a_0^2}\right\} \text{ for } t > 1 + a_0$$

$$Q = K \exp\left\{-\frac{[t - (1 + a_0)]^2}{a_1^2}\right\} \text{ for } t \leq 1 + a_0$$

where, $K = \frac{c_2 \times E(p) \times V(p) \times A(p)}{\alpha_0 + \alpha_1}$, $a_0 = \frac{C_1}{S(p)}$, and $a_1 = \frac{2}{S(p)}$.

The user-specified weld parameters for this heat input model are defined as follows.

- $S(p)$ = weld speed for pass p
- $E(p)$ = arc efficiency for pass p
- $V(p)$ = voltage for pass p
- $A(p)$ = current for pass p

- τ = current time in seconds

Build up time and arrival time are given by:

- Build up time = a_0
- Arrival time = $1 + a_0$

C_1 [mm] affects the duration over which the heat is applied, and C_2 is a dimensionless amplitude scaling parameter.

Although the welding procedure was unknown, typical values for a submerged arc weld (SAW) process with stainless steel weld metal were assumed. For two-dimensional analyses, results may not be sensitive to small variations in specific weld parameters such as voltage, current, pass speed, and the form of the heat input model so long as the total amount of heat input energy is correct and it is applied over an appropriate amount of time [7]. To ensure appropriate heat input, the energy was adjusted for each weld bead by observing the temperature distribution in the surrounding material and tuning the arc efficiencies to obtain a realistic melt zone. The melt zone generally extended between 0.5 mm and 1.5 mm from the edges of each weld bead. A sample plot of the heat input and a temperature contour during weld bead heat-up are shown in Figure 4.

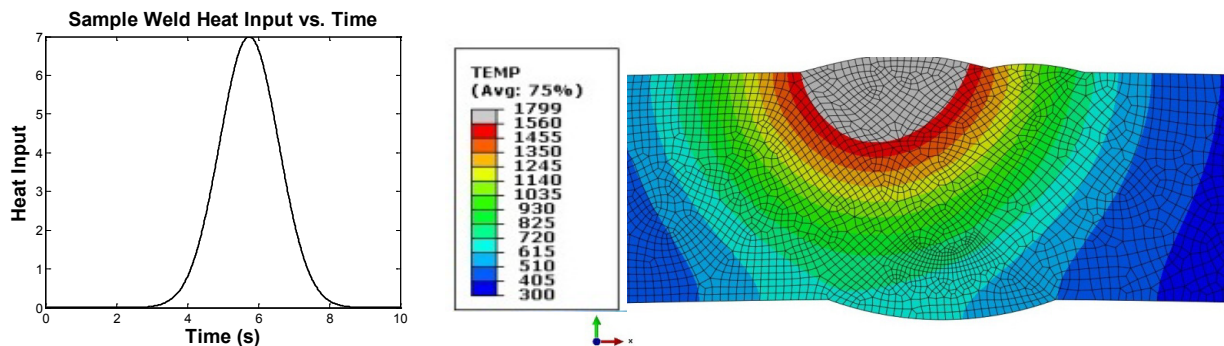


Figure 4: **Left:** Sample heat input function; **Right:** Longitudinal weld pass-5 heat-up temperature profile

4.3 Structural Model

The structural model incorporates the results of the time-dependent temperature loads and performs the deformation calculations that determine the residual stress distribution. Because of the relatively thin vessel wall, boundary conditions were an important consideration in the determination of residual stresses in the weld and adjacent material. In an effort to encompass the actual fabrication constraints, two boundary condition cases were examined for the longitudinal and circumferential canister welds:

- 1) Low Constraint: The cylinder was pinned at the nodes furthest from the weld, indicated by blue squares in Figure 5. Pinning the cylinder at two nodes in these locations prevented only rigid body translation.

- 2) High Constraint: The cylinder was pinned as in (1), with additional radial constraints to simulate fixtures that may be used to prevent deformation during the welding process. The radial constraints prevented all motion in the radial direction at the nodes circled in red in Figure 5. Tangential motion was permitted.

These two boundary condition cases are depicted in Figure 5 for the longitudinal and circumferential weld. Depending on the type and arrangement of weld fixtures used to fabricate a specific canister, weld residual stress results may fall between these two cases. As will be discussed in sections 6.1 and 6.2, the radial constraints had very little effect on the residual stress, so the base plate and lid closure models applied only the low constraint boundary condition.

For the cylinder welds, the back-gouge machining process was modeled as a removal of the affected elements; no heat input was applied. Furthermore, for all welds we assumed that the cylinder was in a zero-stress state initially. Therefore, models did not consider:

- Residual stresses that may be present from the cold-rolling process
- Residual stresses from previous welds, such as weld repairs that may have occurred prior to the longitudinal weld
- Any interaction between the stresses introduced from the longitudinal weld sequence and the stresses introduced from the subsequent circumferential weld sequence

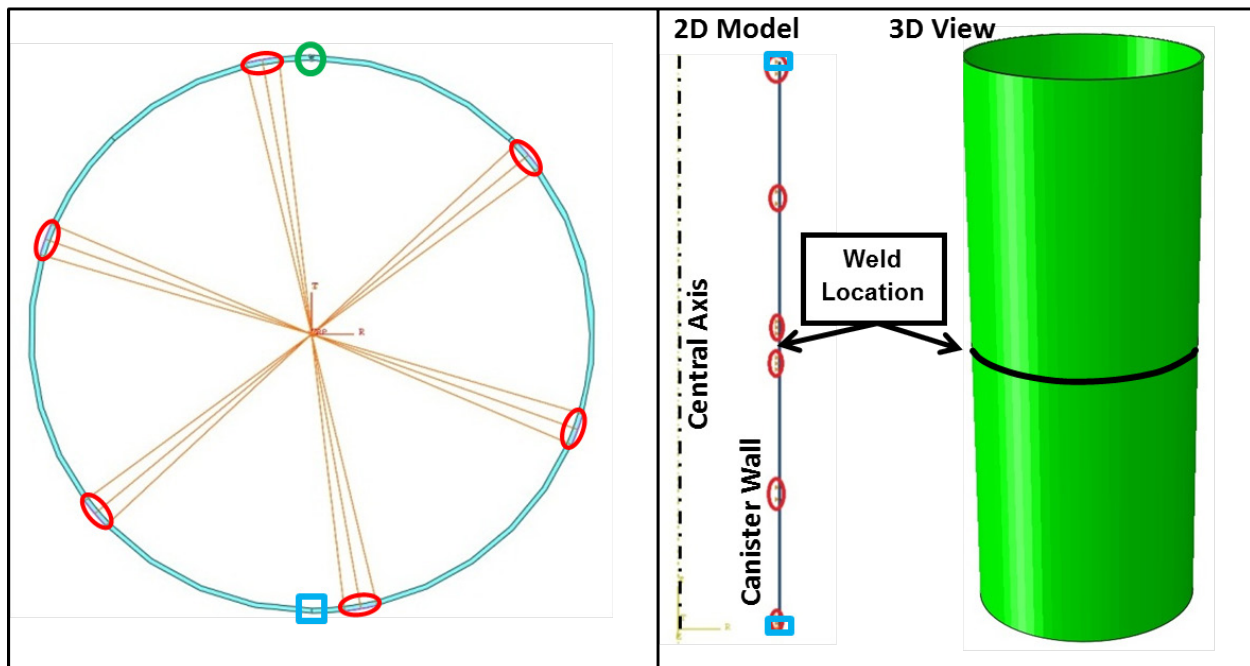


Figure 5: **Left:** 2D longitudinal weld model with radial constraint surfaces indicated by radial lines and circled in red, weld area indicated by green circle, pinned nodes indicated by blue square; **Right:** 2D circumferential weld model with radial constraint surfaces highlighted by red circles, pinned nodes indicated by blue squares. 3D representation is displayed for reference.

Note: Radial constraints were only applied for the high-constraint condition; the low constraint-condition for both the longitudinal and circumferential weld models included only the pinned constraint indicated by blue squares.

5. Benchmarking Analysis

5.1 Literature Review

A literature review was conducted to benchmark weld residual stress estimates and measurements for welds of a similar geometry and material composition as the stainless steel canister. DCSS canisters have a large radius-to-thickness ratio (R/t), generally greater than 50. Most WRS analyses involving stainless steel address piping, which tends to have considerably smaller R/t . Moreover, piping welds involve only the circumferential (girth) butt weld, not a longitudinal weld.

Yaghi et al. [19] performed a parametric study of WRS in thin and thick-walled stainless steel pipe girth welds, varying the inner radius to wall thickness ratio (R_i/t) between 1 and 100. Two different welds were modeled: a 4-pass single-V weld of a pipe with a wall thickness of 7.1 mm, and a 36-pass single-U weld of a pipe with a wall thickness of 40 mm. The authors did not specify the grade of stainless steel, but provided the material properties and described it as steel originally used in boiling water reactor systems. The weld metal yield stress was twice the yield stress of the base material, a notable difference compared to the analysis performed in the current canister work, which uses the same material properties for the weld and base metals. The thin-walled, 4-pass weld is relevant to the canister geometry, so it will be considered. Some results of the study are summarized below:

- Along the weld centerline, the axial residual stress was tensile at the inner surface of the pipe weld, and became compressive toward the outer diameter (OD). Increasing R_i/t significantly reduced the compressive stress on the OD, thereby decreasing resistance to crack initiation at the OD.
- Residual hoop stress along the weld centerline was tensile throughout the wall thickness for R_i/t ratios greater than 1. As R_i/t increased, the through-wall residual stress curves flattened out, and tensile stress on the outer surface grew significantly, increasing susceptibility to crack initiation at the OD.
- Residual through-wall stresses along the HAZ exhibited similar trends.

Brickstad and Josefson [20] performed a similar parametric analysis of stainless steel pipe girth welds. In addition to pipe size (thickness and number of passes) and R/t ratio, their sensitivity analysis included variations in weld metal yield stress, interpass temperature, and net line energy, Q . Q is a heat flux quantity defined by welding electrode travel speed, voltage, current, and arc efficiency. For a 4-pass weld, the analysis included only an R_i/t of 4.4, but nevertheless the trends were similar to those in Yaghi's analysis [19]: high tensile residual hoop stress throughout the wall thickness at the weld centerline, and axial through-wall residual stress transitioning from tensile on the inner surface to compressive on the outer surface. Decreasing the net line energy of the weld increased the through-wall hoop stress throughout the thickness, shifting the stress curves up. For a 14-pass stainless steel pipe girth weld, hoop stress in the heat affected zone became significantly more tensile through the wall and toward the outside surface as R_i/t increased from 8.3 to 30 [20].

Another study performs three-dimensional finite element analysis on the circumferential weld of thin-walled SAE 1020 carbon steel piping [21]. While the material affects the stress magnitude, the through-thickness residual stress trends are similar to those found in the aforementioned analyses. The authors also present stress results along the length of the pipe, moving away from the weld, a feature that is not available in the axisymmetric, two-dimensional analyses.

Finally, a recent study was chosen for a benchmarking analysis because it calculated weld residual stresses in a stainless steel pipe girth weld analytically and also provided experimental validation [14]. The pipe, which had a diameter of 369 mm and a wall thickness of 40 mm, was relatively thick-walled and much smaller in diameter in comparison with a DCSS canister, but provides a point of comparison for the circumferential butt weld of a cylindrical geometry constructed from stainless steel base-metal. The weld was of a single-V configuration with Alloy 82 weld metal deposited in 25 passes using the tungsten inert gas process. The material properties and exact weld geometry used in the reference were not specified, so the weld pass geometry was approximated based on the drawings provided [14], and material properties for stainless steel and Alloy 182 from previously developed weld residual stress analysis models were applied [8]. The benchmarking analysis conducted by the NRC will be designated as BA, while the comparative analysis from [14] is referred to as CA. Figure 6 shows the BA model weld cross-section.

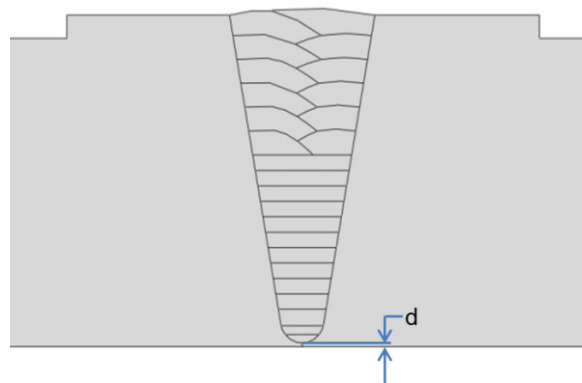


Figure 6: Benchmarking model weld geometry BA

Figure 7 and Figure 8 contain plots comparing the through-wall weld residual stress along the weld centerline derived with the analysis procedure BA to the stresses measured and calculated in CA. Stresses are plotted for each of the two analyses using isotropic and kinematic material hardening laws. The plots overlay the results from analysis BA with selected digitized results from CA. Note that the results from CA contain three distinct sets of data. The first, FNC, is from a weld residual stress analysis carried out in ABAQUS[®] finite element software by Frazer Nash Consultancy. The second, DHD, represents the experimental stress measured using the deep hole drilling technique at three circumferential locations on the weld: 35°, 125°, and 225°. Finally, the UoB (University of Bristol) stresses are from a virtual DHD obtained by mapping the axisymmetric FNC stresses onto a 3D mesh.

5.2 Axial Stress

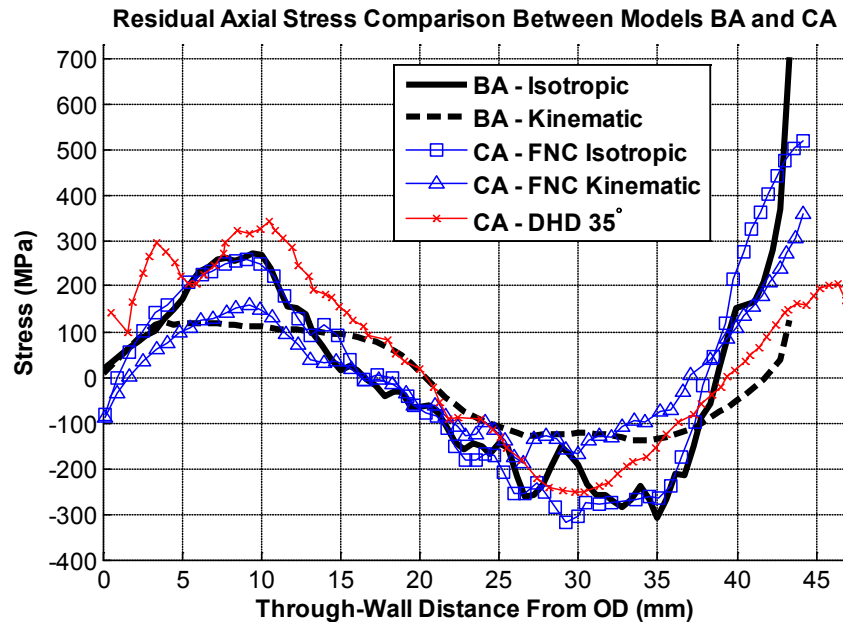


Figure 7: Pipe benchmarking weld residual axial stress comparison

Isotropic hardening axial stress from BA coincides very closely with the CA study, generally following the CA results. The axial stress on the ID is exceedingly high in BA, likely because the land upon which the first weld pass was applied was very thin: 0.5 mm, marked as dimension d in Figure 6. Increasing the land thickness, d , to more closely match the apparent thickness shown in CA may bring the stress on the ID surface close to the FNC prediction of 500 MPa. The isotropic hardening analysis results from both studies more closely followed the DHD measured axial stress until approximately the final 5 mm of material (depths between 38 and 43 mm), where the stress calculated with kinematic hardening better predicted the DHD measured stress. Kinematic hardening results of analysis BA followed a similar trend as the CA predictions with kinematic hardening but were about 25 to 75 MPa more tensile in the 13 to 23 mm depth range and were more compressive from 33 mm deep to the ID. However, the axial stress with kinematic hardening from analysis BA more closely matches the DHD measurements close to the ID.

5.3 Hoop Stress

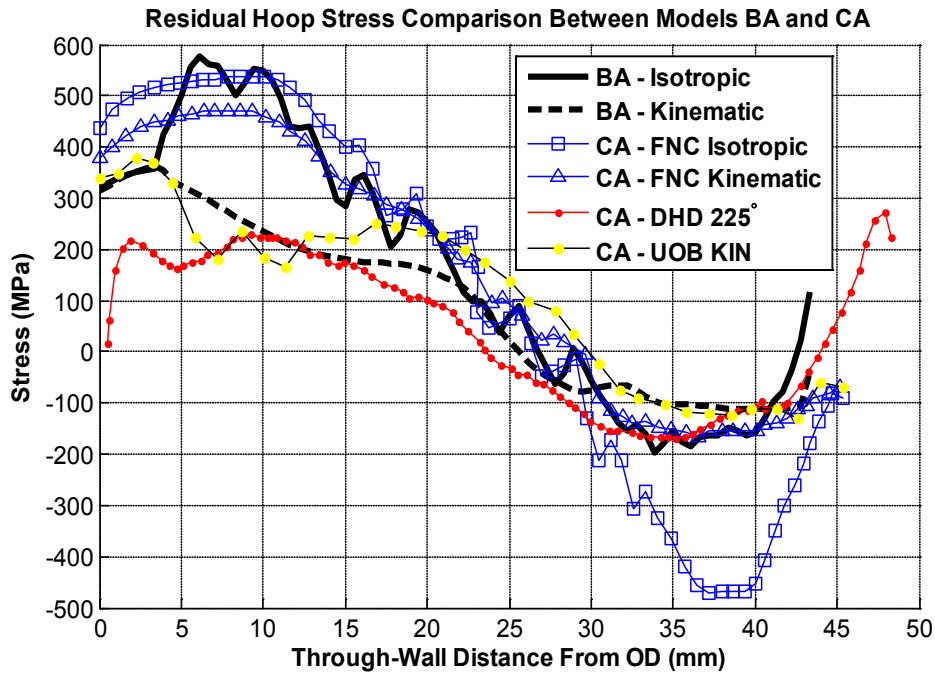


Figure 8: Pipe benchmarking weld residual hoop stress comparison

Hoop stress for the isotropic hardening models BA and CA followed very closely from a depth of 5 mm to 30 mm from the OD, after which the stress from model BA was far less compressive than CA and more closely matched the 225 degree DHD measurement. Isotropic hardening hoop stress calculations from BA between the OD surface and a depth of 4 mm were roughly in the middle of the 225 degree DHD measurement and the isotropic hardening hoop stress from CA, and were close to the UoB values. Model BA hoop stresses for kinematic hardening were more closely correlated with the DHD 225 degree measurement and the UoB kinematic hardening results. The model BA isotropic hardening results were close to the 225 degree DHD measurement for ID hoop stress.

In both the axial and hoop stress components, the largest discrepancies between model BA and model CA's predictions occur on the pipe wall surfaces. In general, the results acquired using the analysis method applied in this paper were in good agreement with measurements and analysis from [14]. Therefore, these techniques are considered to be adequate for the purposes of estimating the weld residual stresses for the DCSS canisters.

6. Canister WRS Analysis Results

The following sections contain the structural analysis results for the four canister welds analyzed in this work: the circumferential and longitudinal canister butt welds, and the base plate and lid closure welds. Results are presented as stress contour images, as well as through-wall stress profiles where the stress along a path through the component has been extracted and plotted versus the distance along the path.

6.1 Circumferential Weld

The final axial and hoop residual stress contours for the canister circumferential weld are plotted in Figure 9 through Figure 12. Note that contour plots of axial stress, Figure 9 and Figure 10, are on a different scale than plots of hoop stress, Figure 11 and Figure 12. Stress contours are displayed for the both the high and low constraint cases (with and without radial constraints, respectively), as well as for the two hardening laws, isotropic and kinematic, for a total of 8 images. Note that the right side of the contours is the outside surface of the canister; attention will be focused on the outside surface due to the potential for chloride deposition in those areas. Each image shows an expanded view of the canister wall, as well as a magnified view near the weld. The weld outline is shown with a dashed black line for reference.

For both the circumferential and longitudinal canister welds, stress along one of the three through-wall paths shown in Figure 13 was plotted based on which path contained the most conservative value of stress (highest tensile stress) on the outer surface of the canister wall; results for the circumferential weld are shown in Figure 14. The legend in those plots indicates the hardening law (isotropic or kinematic), followed by the stress component (hoop or axial) and the through-wall path along which the stress was calculated (left, center, or right as shown in Figure 13). The horizontal axis on the through-wall stress profile plots is a measure of the distance along the path, starting from the outside surface of the canister.

The through-wall stresses displayed in Figure 14 exhibit similar trends to the thin-walled stainless steel cylinder weld analyzed in [19] for this geometry's radius-to-thickness ratio of approximately 50. Note that both the isotropic and kinematic hardening laws result in hoop stresses through the weld which are tensile and are above the yield strength of the material.

6.1.1 Axial Stress

Figure 14 shows that the radial constraints applied in this analysis had very little effect on the surface or through-wall stress in the weld or heat affected zone. Isotropic and kinematic hardening properties resulted in very similar through-wall residual stress, with the outer surface of the weld in compression. All four models (isotropic and kinematic hardening with and without radial constraints) resulted in the largest tensile stresses occurring in a 30 to 40 mm band approximately 90 mm symmetrically from the weld centerline on the outside surface of the canister. Stress predictions in these areas were between 110 and 209 MPa without radial constraints, and between 158 MPa and 228 MPa with radial constraints.

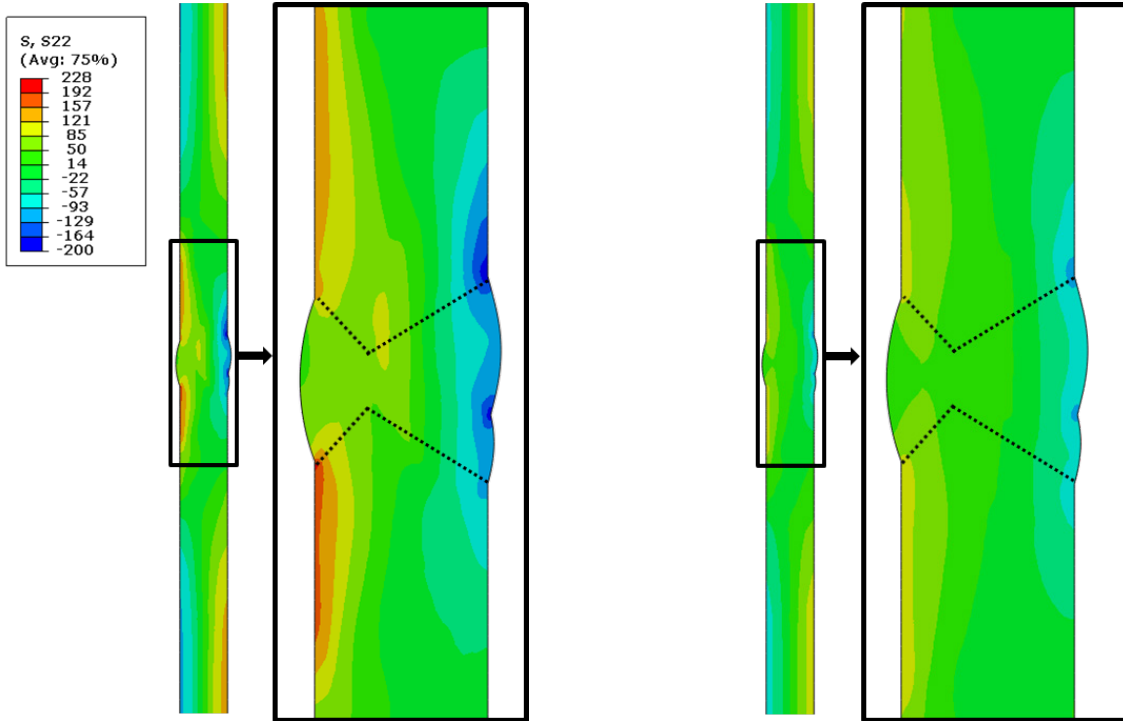


Figure 9: Circumferential weld residual axial stress contour without radial constraints;
Left: Isotropic hardening; **Right:** Kinematic Hardening

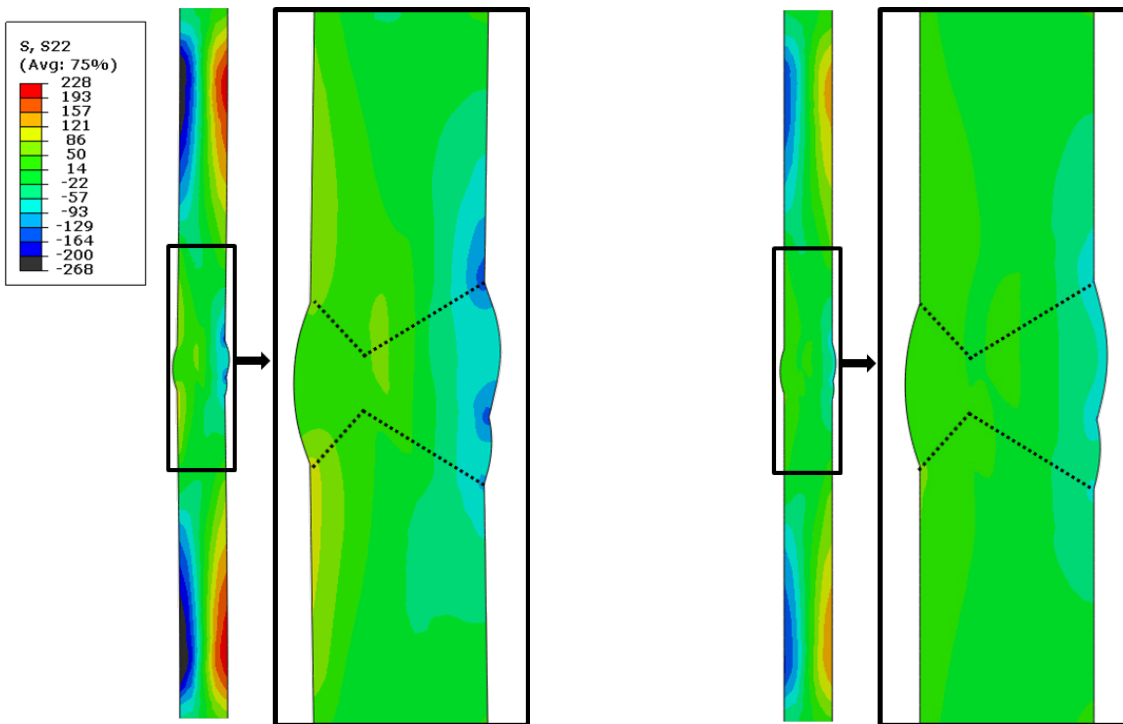


Figure 10: Circumferential weld residual axial stress contour with radial constraints;
Left: Isotropic hardening; **Right:** Kinematic Hardening

6.1.2 Hoop Stress

Again, the through-wall stress profiles (Figure 14) illustrate that radial constraints had a very small effect on the through-wall residual stress in the weld and heat-affected zone. The highest outer surface tensile residual stresses occurred in the weld or heat affected zone. Kinematic hardening models resulted in outer surface residual stresses that were more than 100 MPa lower than the isotropic hardening results. The highest outer surface tensile residual stresses were between 220 MPa and 390 MPa and extended approximately 40 mm to either side of the weld centerline. Note that the maximum hoop stresses occurred in or near the weld and were tensile through the entire thickness, which has important implications on crack growth. The through-wall tensile stress extended approximately 30 mm to either side of the weld centerline. Moreover, the hoop stress remained very near to or above yield along the chosen paths through the thickness of the canister weld for all cases analyzed: high constraint, low constraint, isotropic hardening, and kinematic hardening.

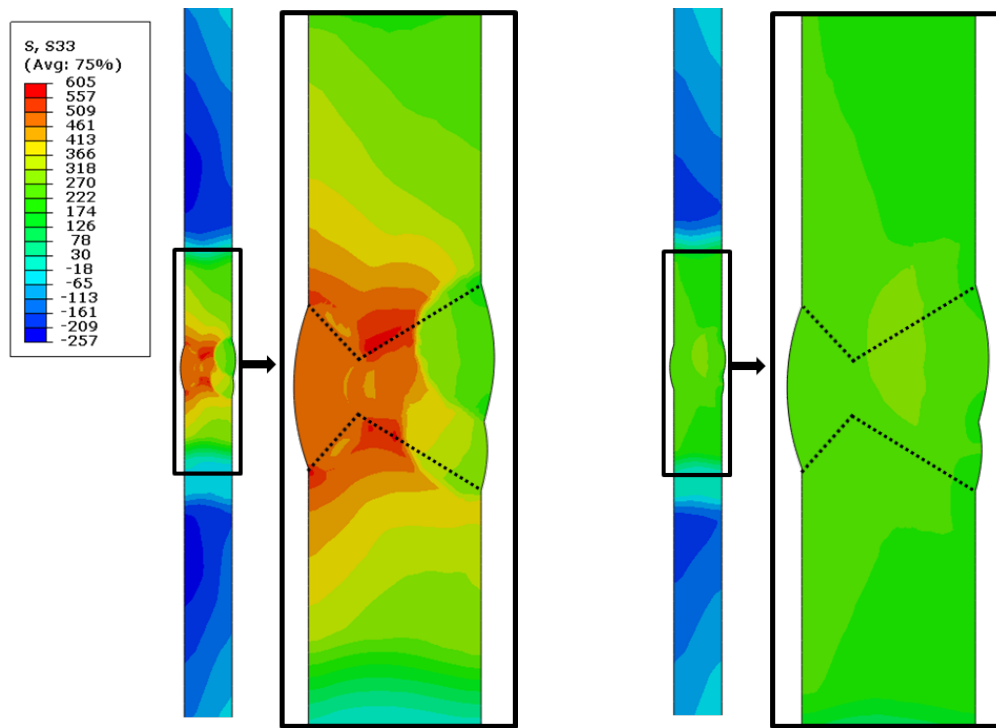


Figure 11: Circumferential weld residual hoop stress contour without radial constraints;
Left: Isotropic hardening; **Right:** Kinematic Hardening

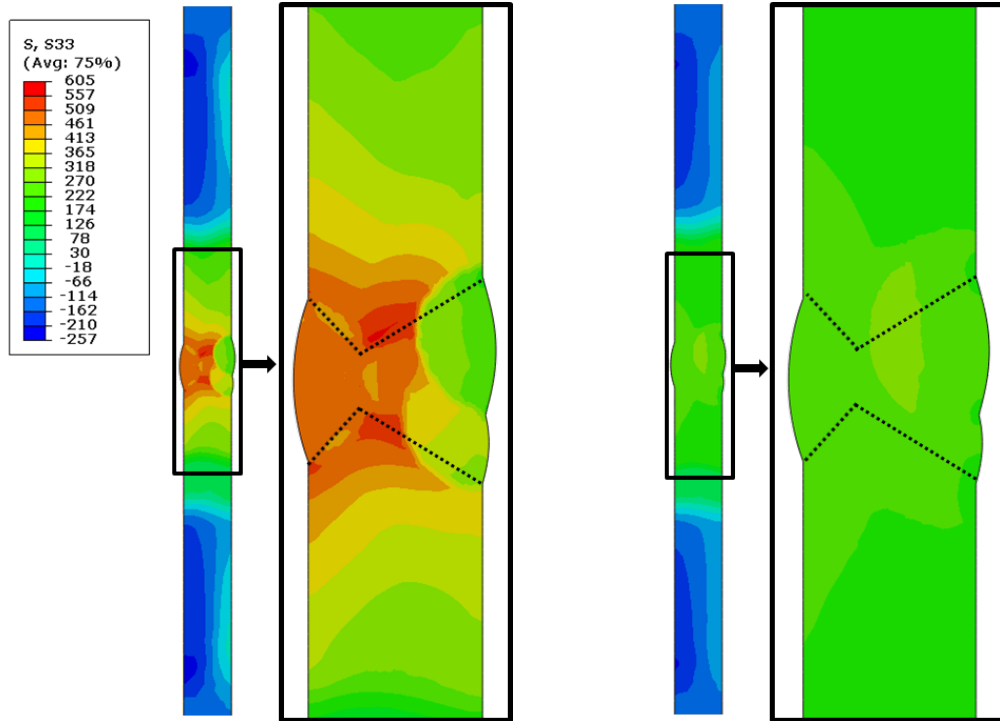


Figure 12: Circumferential weld residual hoop stress contour with radial constraints;
Left: Isotropic hardening; **Right:** Kinematic Hardening

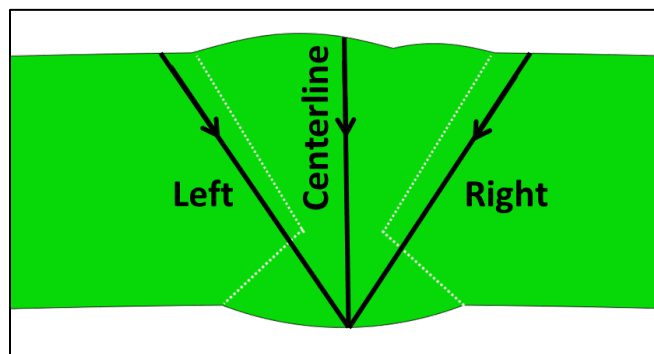


Figure 13: Paths along which through-wall stresses are plotted for the circumferential and longitudinal canister butt welds

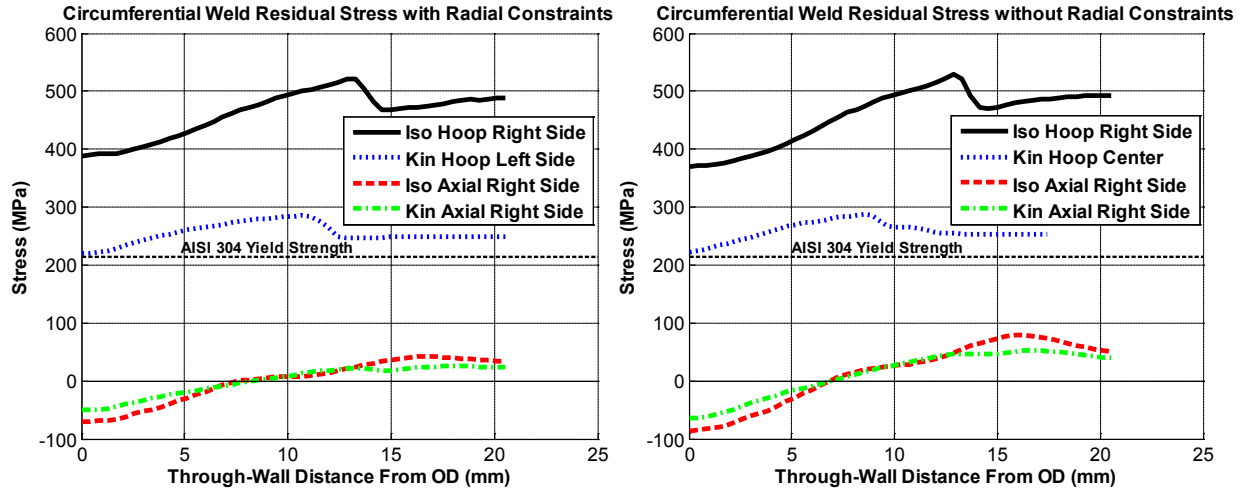


Figure 14: Circumferential Weld Through-Wall Residual Stress; **Left:** With radial constraints; **Right:** Without radial constraints

6.2 Longitudinal Weld

The final axial and hoop residual stress contours for the canister longitudinal weld are plotted in Figure 15 and Figure 16, respectively. Note that contour plots of axial stress are on a different scale than plots of hoop stress. Stress contours are displayed for both the high and low constraint cases (with and without radial constraints, respectively), as well as for the two hardening laws, isotropic and kinematic, for a total of 8 images. Note that the top side of the contours is the outside surface of the canister. The weld outline is plotted with a dashed black line for reference. The through-wall stresses are plotted in Figure 17. Note that both the isotropic and kinematic hardening laws result in axial stresses through the weld which are tensile and are above the yield strength of the material.

6.2.1 Axial Stress

Unlike the circumferential weld, the longitudinal weld resulted in residual stresses with a larger axial than hoop component. Axial stress was fairly insensitive to the radial constraints; however, there were large differences in residual stress depending on the hardening law applied. The largest outer surface tensile residual stresses were between 450 MPa and 480 MPa with isotropic hardening, and were about 300 MPa with kinematic hardening. The outer surface tensile stress extends approximately 50 mm from either side of the weld centerline, while the through-wall tensile stress extends approximately 45 mm from either side of the weld centerline. The axial stress remained very near to or above yield along the chosen paths through the thickness of the canister weld for all cases analyzed: high constraint, low constraint, isotropic hardening, and kinematic hardening.

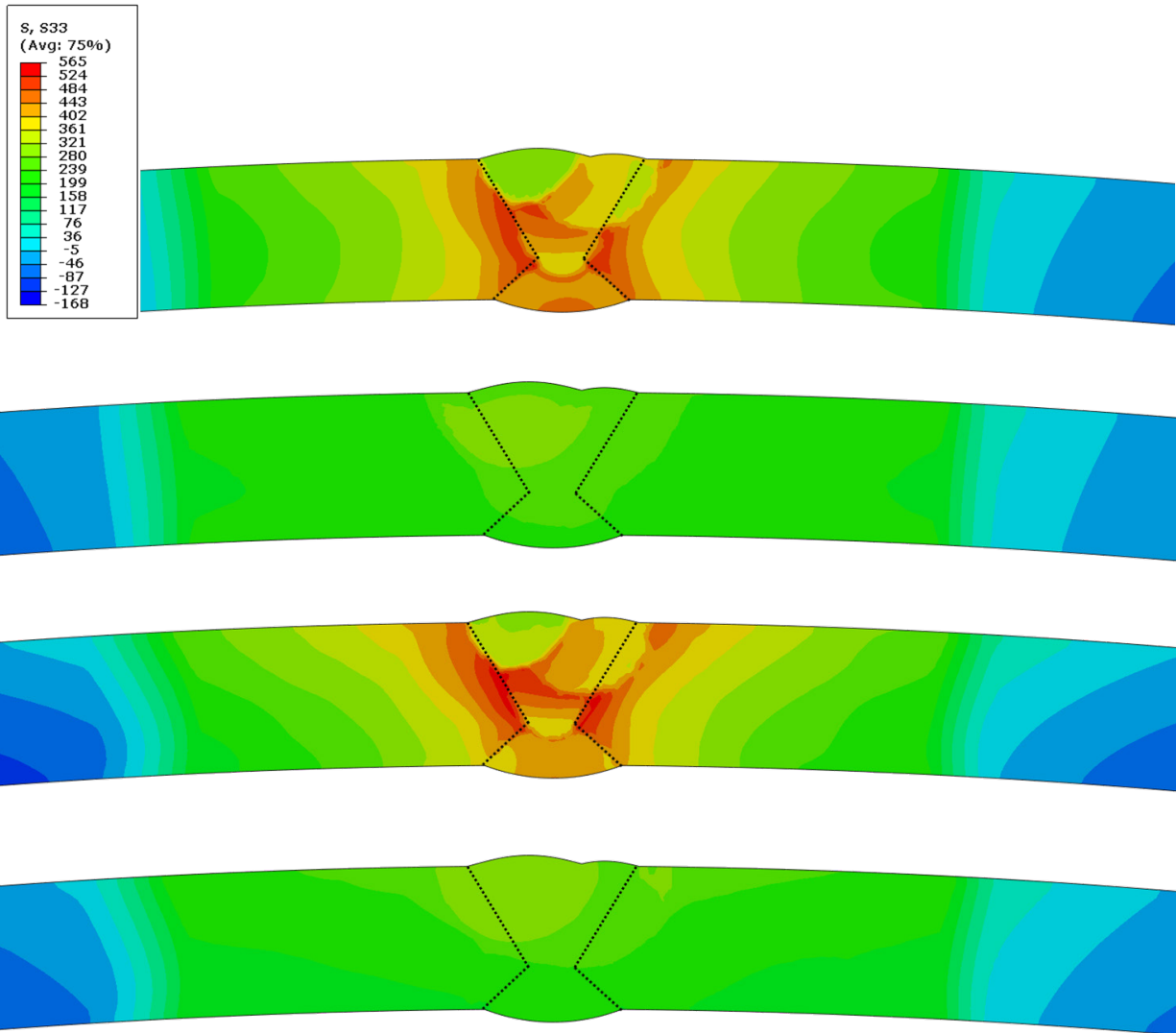


Figure 15: Longitudinal weld residual axial stress; Top to bottom: (1) Without radial constraints, isotropic hardening; (2) Without radial constraints, kinematic hardening; (3) With radial constraints, isotropic hardening; (4) With radial constraints, kinematic hardening

6.2.2 Hoop Stress

Residual stresses in the hoop direction were up to 6 times lower than in the axial direction and were more affected by the radial constraint. With radial constraints applied, hoop residual stresses increased by close to 100% on the outer surface between the constrained nodes and the weld, as well as through the weld and heat affected zone. The largest outer surface tensile residual stresses were between 96 MPa and 136 MPa with radial constraints, compared to 70 MPa without constraints.

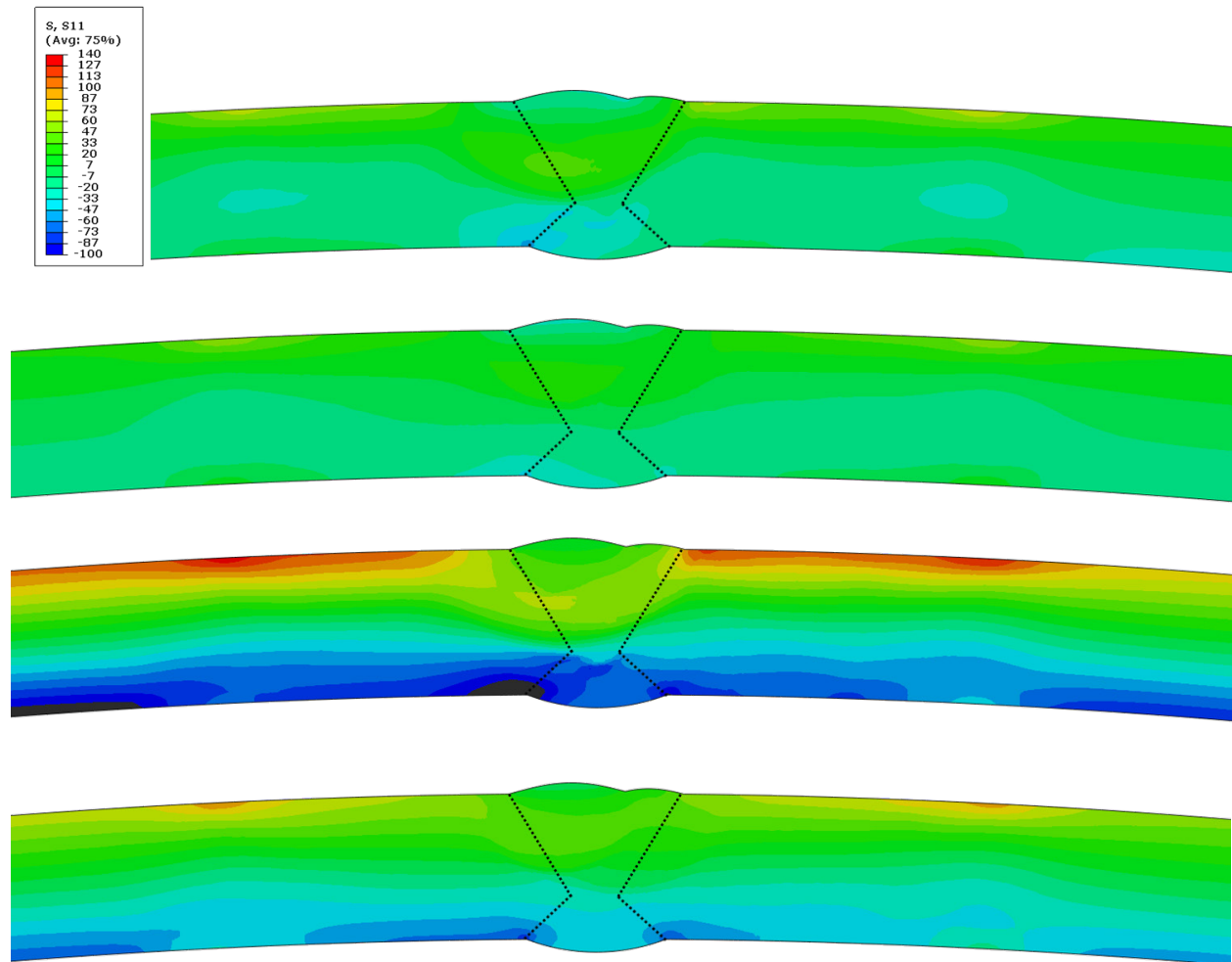


Figure 16: Longitudinal weld residual hoop stress; Top to bottom: (1) Without radial constraints, isotropic hardening; (2) Without radial constraints, kinematic hardening; (3) With radial constraints, isotropic hardening; (4) With radial constraints, kinematic hardening

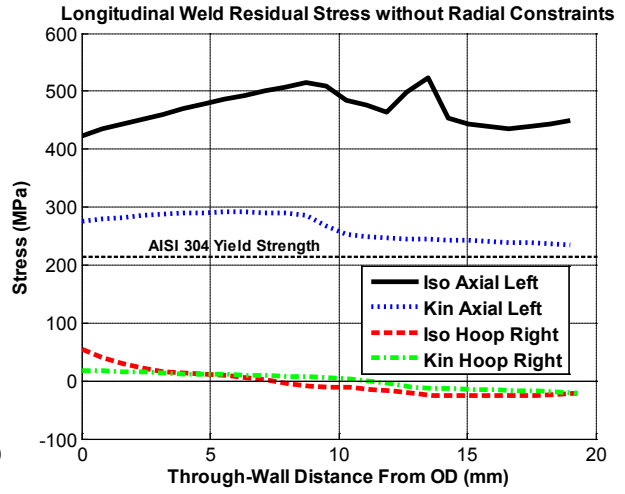
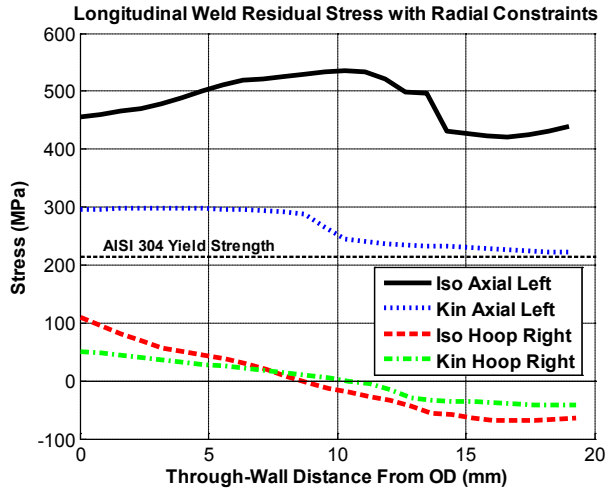


Figure 17: Longitudinal weld through-wall residual stress; **Left:** With radial constraints; **Right:** Without radial constraints

6.3 Base Plate Weld

As was performed for the circumferential and longitudinal butt welds, residual stress is summarized in contour images and plots along paths chosen in and near the weld. Figure 18 shows the through-weld, base plate surface, and cask wall surface paths. Note that the wall and base surface paths extend in straight-lines beyond what is shown, for a total distance of 500 mm. Figure 19 displays stress contours for simulations using isotropic and kinematic hardening and for each normal stress component: s_{xx} , s_{yy} , and s_{zz} . These are denoted s_{11} , s_{22} , and s_{33} , respectively, in the figure. Each of those plots also contains an indicator of the x (horizontal) and y (vertical) directions, and z protrudes out of the plane of the page. Figure 20 displays the stress for the directional component that achieved relatively high, tensile values along a particular path. The stress components are indicated in the figure legend.

The z component of the through-weld residual stress was high and tensile, exceeding the material yield strength from the outer surface through to a depth of about 22 mm, as indicated in Figure 20(a), and remaining tensile throughout the thickness of the base plate along the chosen path. The stress predicted at the surface is within 25 MPa for the isotropic and kinematic hardening models, but differs widely at greater depths into the base plate. The stress predictions from the isotropic hardening model are in some places more than twice those of the kinematic hardening model. Stress in the z direction was also high and tensile along the base outer surface for a distance of approximately 50 mm, and along the cask wall outer surface for about 30 to 40 mm, as indicated in Figure 20(b) and (c), respectively.

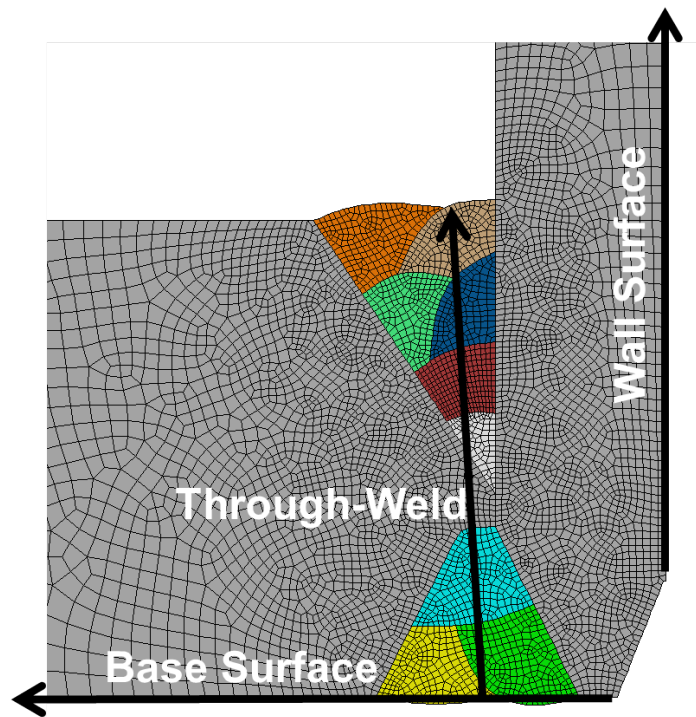


Figure 18: Paths for Base Plate Stress Plots

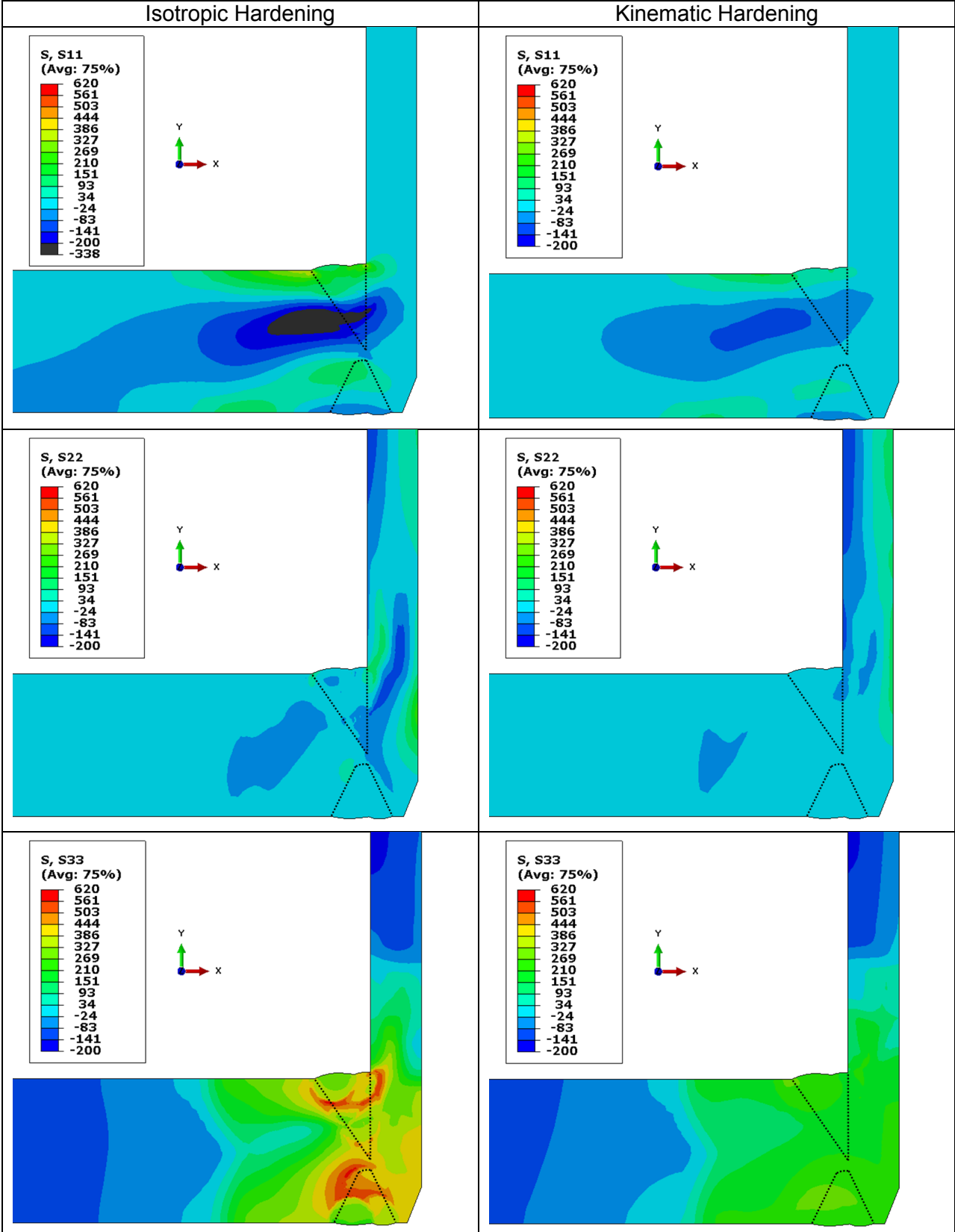
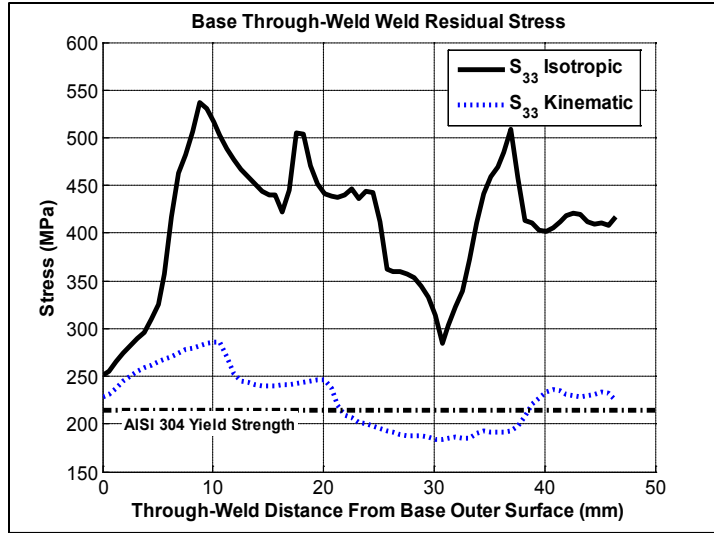
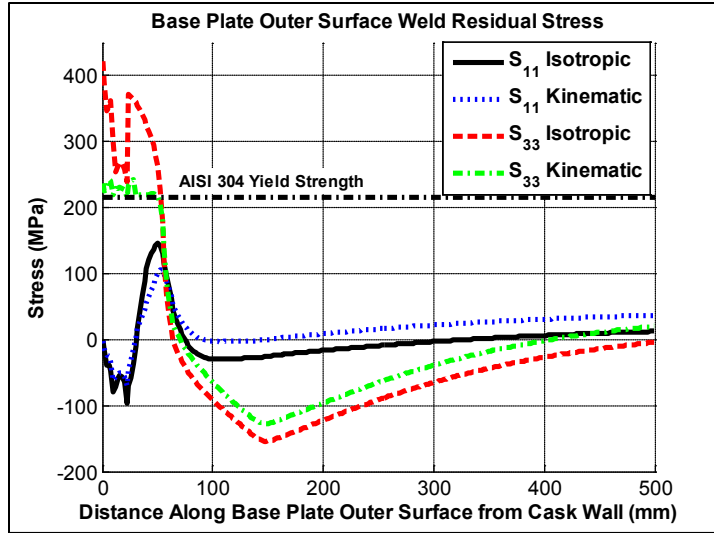


Figure 19: Base plate weld contours; Left: Isotropic Hardening; Right: Kinematic Hardening

(a)



(b)



(c)

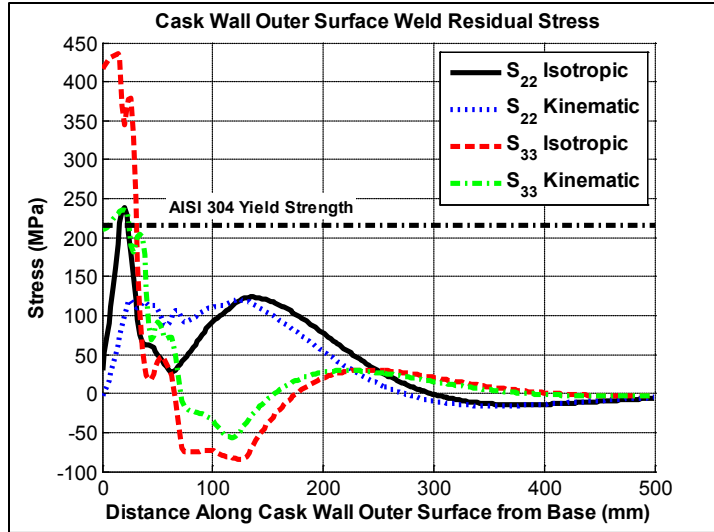


Figure 20: Base plate stress along paths: (a) Through-weld; (b) Base plate outer surface; (c) Cask wall outer surface

6.4 Lid Closure Weld

Again, residual stress is summarized in contour images and plots along paths chosen in and near the weld. Figure 21 shows the through-weld, lid surface, and cask wall surface paths. Note that the wall and lid surface paths extend in straight-lines beyond what is shown, for a total distance of 500 mm. Figure 22 displays stress contours for simulations using isotropic and kinematic hardening and for each normal stress component: s_{xx} , s_{yy} , and s_{zz} . These are denoted s_{11} , s_{22} , and s_{33} , respectively, in the figure. Each of those plots also contains an indicator of the x (horizontal) and y (vertical) directions, and z protrudes out of the plane of the page. Figure 23 displays the stress for the directional component that achieved relatively high, tensile values along a particular path.

The through-weld residual stress was high and tensile in the z direction, exceeding the material yield strength from the outer surface through approximately 75% of the thickness in the case of kinematic hardening, and throughout the entire thickness using the isotropic hardening law, as indicated in Figure 23(a). As with the base plate weld, the predicted stress in the z direction varies widely depending on the material hardening law; however, both models predict tensile stress throughout the thickness of the lid at the weld centerline. Stress in the z direction was also high and tensile along the lid outer surface for a distance of approximately 50 mm, and along the cask wall outer surface for about 30 to 40 mm, as indicated in Figure 23(b) and (c), respectively.

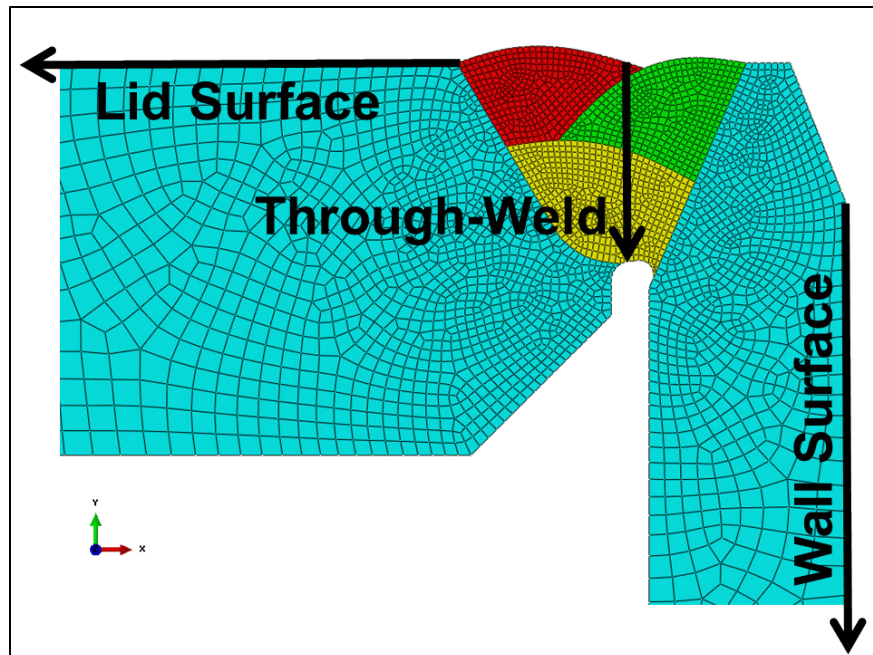


Figure 21: Paths for Lid Stress Plots

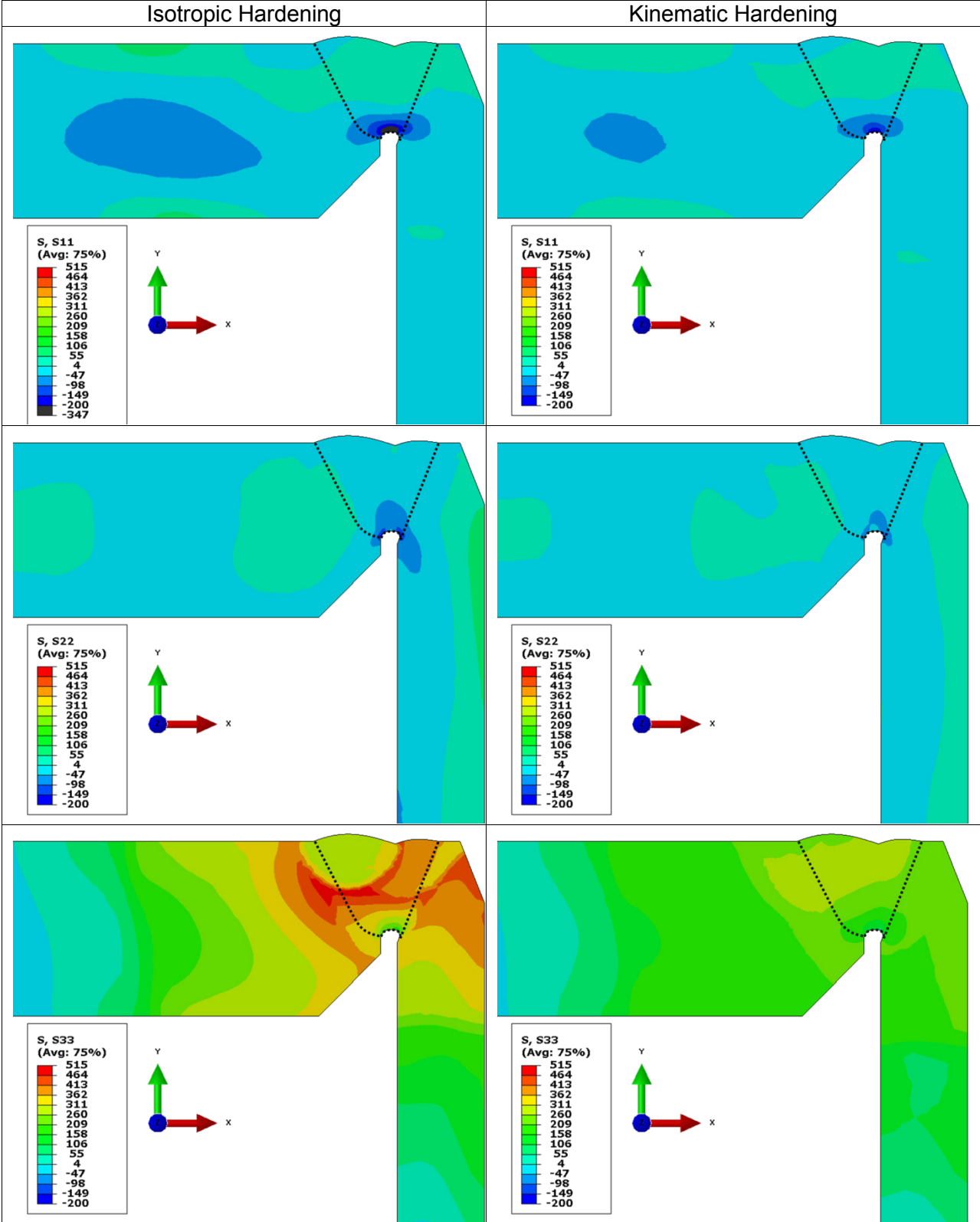


Figure 22: Lid weld contours; **Left**: Isotropic Hardening; **Right**: Kinematic Hardening

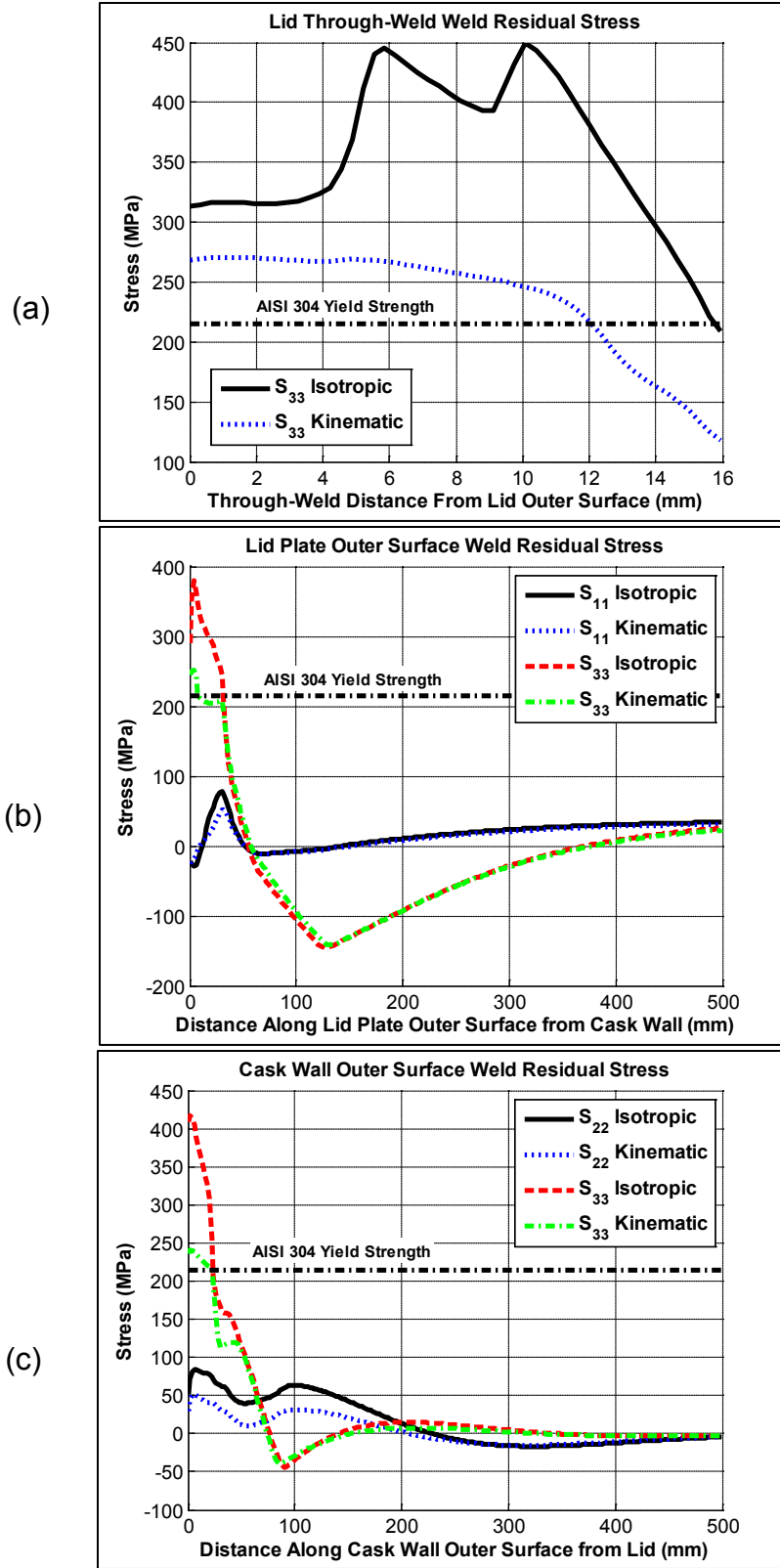


Figure 23: Lid stress along paths: (a) Through-weld; (b) Lid outer surface; (c) Cask wall outer surface

7. Summary

Finite element analyses were conducted to benchmark analytical methods and then evaluate the weld residual stresses in the longitudinal and circumferential welds of a representative DCSS canister. Models included both isotropic and kinematic hardening laws, and the cylinder circumferential and longitudinal butt welds considered a low and high constraint condition which simulated possible weld fixtures. The applied constraints had relatively little effect on the stress results in comparison to the large differences exhibited by applying the two different hardening rules. The benchmarking analysis of a stainless steel pipe butt weld showed good agreement in both trend and magnitude with experimental and analytical stress results from the published study [14]. The circumferential storage canister weld resulted in high tensile hoop stresses in the weld and heat affected zone, remaining near or above yield stress throughout the thickness of the canister. The longitudinal weld induced high tensile residual stresses in the axial direction, also remaining near or above yield stress throughout the thickness of the canister. Both the longitudinal and circumferential results suggest that a potential chloride-induced SCC indication would have a tendency to grow perpendicular to the weld direction, but would reach a region of compressive stress approximately 40 mm from the weld centerline. Similarly, for the base plate and lid closure welds, surface stress tended to become compressive or zero within a distance of approximately 50 mm from the weld. The calculated residual stresses in at least one component direction in the circumferential, longitudinal, base plate, and lid closure welds were tensile through the full thickness of the canister in and near the weld; this would have deleterious effects on potential crack growth since there are no compressive regions to slow or arrest through-wall growth.

A more extensive three-dimensional analytical model that considered fabrication stresses, assessed the interaction between various welds and included a corresponding experimental program would be beneficial to refine the understanding of surface and through-wall weld residual stresses. Several assumptions were made about the weld geometry; welding and fabrication induced stresses measured on a representative DCSS canister or appropriately designed mock-up would be helpful to provide validation of these results. However, these results, in combination with existing literature which shows CISCC initiation in stainless steel specimens strained to stresses at [5] and below [22] yield, indicate that there may be sufficient stress for chloride-induced SCC to occur in DCSS canisters in susceptible environments. Based on this analysis, we would suspect that an initiated chloride induced stress corrosion crack could grow through-wall.

References

1. US NRC Office of Nuclear Material Safety and Safeguards, "NRC Information Notice 2012-20: Potential Chloride Induced Stress Corrosion Cracking of Austenitic Stainless Steel and Maintenance of Dry Cask Storage System Canisters," Washington, DC, November 14, 2012.
2. King, C., Waldrop, K., "EPRI RIRP Issue Update: Chloride Induced Stress Corrosion Cracking of Spent Fuel Canisters," Industry-NRC Meeting on Stainless Steel Canister Degradation Issues, Rockville, MD, ML13022A316, December 18, 2012.
3. Oberson, G., Dunn, D., Mintz, T., He, X., Pabalan, R., Miller, L., "US NRC-Sponsored Research on Stress Corrosion Cracking Susceptibility of Dry Storage Canister Materials in Marine Environments – 13444," Waste Management Conference, 2013.
4. Kain, R., 1990, "Marine Atmospheric Stress Corrosion Cracking of Austenitic Stainless Steel," *Materials Performance*, 29(60)
5. Oberson, G., Dunn, D., et al., "U.S. NRC Sponsored Research on Stress Corrosion Cracking Susceptibility of Dry Storage Canister Materials in Marine Environments," 2013 Waste Management Symposium Presentation, Phoenix, AZ, February 24-28 2013.
6. Crooker, P., Broussard, J., 2011, "Materials Reliability Program: Finite-Element Model Validation for Dissimilar Metal Butt-Welds (MRP-316)," 1022861, Electric Power Research Institute, Palo Alto, CA
7. H. J. Rathbun, L. F. Fredette, P. M. Scott, A. A. Csontos, and D. L. Rudland, "NRC Welding Residual Stress Validation Program International Round Robin Program and Findings," *Proceedings of the ASME Pressure Vessels and Piping Conference*, Baltimore, MD, PVP2011-57642, July 2011.
8. Fredette, L. F., Kerr, M., Rathbun, H. J., Broussard, J. E., "NRC/EPRI Welding Residual Stress Validation Program: Phase III Details and Findings," *Proceedings of ASME Pressure Vessels and Piping Division Conference*, PVP 2011-57645, 2011.
9. M. Kerr, D. L. Rudland, M. B. Prime, H. Swenson, M. A. Buechler, and B. Clausen, "Characterization of a Plate Specimen from Phase I of the NRC/EPRI, Weld Residual Stress Program," *Proceedings of the ASME Pressure Vessels and Piping Conference*, Baltimore, MD, PVP2011-57687, July 2011.
10. Crooker, P., Broussard, J., 2011, "Materials Reliability Program: Welding Residual Stress Dissimilar Metal Butt-Weld Finite Element Modeling Handbook (MRP-317)," 1022862, Electric Power Research Institute, Palo Alto, CA
11. Kessler, J., 2010, "Industry Spent Fuel Storage Handbook," 1021048, Electric Power Research Institute, Palo Alto, CA

12. Lemaitre, J., and Chaboche, J. L., "Mechanics of Solids", Cambridge University Press, Chapter 5, 1990.
13. ABAQUS User Manual, Simulia, Dassault Systems, version 6.11-1, 2011.
14. Ogawa, K., et al, "The Measurement and Modelling of Residual Stresses in a Stainless Steel Pipe Girth Weld," Proceedings of ASME Pressure Vessels and Piping Division Conference, PVP 2008-61542, 2008.
15. J. Goldak, A. Chakravarti, and M. Bibby, "A New Finite Element Model for Welding Heat Sources," Metallurgical Transactions B, Vol. 15B, 1984, pp. 299-305.
16. Z. Feng, K. Wolfe, and E. Willis, "A Computational Modeling Tool for Welding Repair of Irradiated Materials," 19th International Conference on Nuclear Engineering, May 16-19, 2011, Chiba, Japan, ICONE19-44103.
17. B. Taljat, T. Zacharia, X.-L. Wang, J. R. Keiser, R. W. Swinderman, Z. Feng, and M. J. Jirinec, "Numerical Analysis of Residual Stress Distribution in Tubes with Spiral Weld Overlay," Welding Journal, Vol. 77, 1998, pp. 328s-335.
18. Z. Feng, "A Computational Analysis of Thermal and Mechanical Conditions for Weld Metal Solidification Cracking," Welding in the World, Vol. 33, 1994, pp. 340-347.
19. Yaghi, A., Hyde, T., Becker, A., Sun, W., Williams, J., 2006, "Residual Stress Simulation in Thin and Thick-Walled Stainless Steel Pipe Welds Including Pipe Diameter Effects," International Journal of Pressure Vessels and Piping, **83**(864-874), ISSN 0308-0161.
20. Brickstad, B., B.L. Josefson, 1998, "A parametric study of residual stresses in multi-pass butt-welded stainless steel pipes," International Journal of Pressure Vessels and Piping, **75**(11-25).
21. Tso-Liang Teng, Peng-Hsiang Chang, 1997, "A study of residual stresses in multi-pass girth-butt welded pipes," International Journal of Pressure Vessels and Piping, **74**(59-70).
22. Mayuzumi, M., Tani, J., Arai, T., 2008, "Chloride induced stress corrosion cracking of candidate canister materials for dry storage of spent fuel," Nuclear Engineering and Design, **238**(1227-1232).